npj Natural Hazards

https://doi.org/10.1038/s44304-026-00255-y

Article in Press

Building damage assessment in storm-induced disasters using multi-source remote sensing data and NBDANet

Received: 26 January 2026

Accepted: 31 July 2026

Published online: 14 August 2026

Cite this article as: Yang, Y., Fang, J., Yu, X. *et al.* Building damage assessment in storm-induced disasters using multi-source remote sensing data and NBDANet. *npj Nat. Hazards* (2026). https://doi.org/10.1038/s44304-026-00255-y

Yangyang Yang, Jiayi Fang, Xiao Yu, Wanchao Bian, Haiping Xia, Xie Hu & Tangao Hu

Building Damage Assessment in Storm-Induced Disasters Using Multi-source Remote Sensing Data and NBDANet

Yangyang Yang [1, 2], Jiayi Fang [1, 2, *], Xiao Yu [3], Wanchao Bian [1, 2], Haiping Xia [1, 2], Xie Hu [4], and Tangao Hu [1, 2]

Abstract—**Rapid identification of building damage distribution during the critical rescue phase is essential for efficient emergency response. However, most existing studies focus on earthquake-like structural hazards, limiting their generalization across different disaster scenarios. In addition, current methods often struggle to effectively integrate cross-temporal features from pre- and post-disaster imagery, while effective links between pixel-level classification and regional decision-making information remain limited. To address these issues, this study proposes an improved deep learning framework, NBDANet, developed based on BDANet for building damage assessment. NBDANet adopts a two-stage architecture with Spatial Pyramid Pooling (SPP) modules embedded in both stages to enhance multi-scale contextual representation. The first stage performs building localization, while the second stage introduces a Dual-input Triplet Attention (DTA) module to improve feature interaction between pre- and post-disaster images and enhance damage classification accuracy. The model is trained and evaluated on the xBD dataset and further applied to the Derna case using high-resolution GeoEye-1 imagery. Validation is supplemented by Sentinel-derived Normalized Difference Built-up Index (NDBI) and Damage Proxy (DP) maps, confirming spatial consistency. In addition, Global Human Settlement Layer (GHSL) data are integrated to estimate affected populations and delineate rescue-priority zones. Results show that 22% of buildings were damaged, including approximately 20% of all buildings classified as *Major damage* or *Destroyed*. Estimated affected populations in *Major damage* and *Destroyed* zones were approximately 5,200 and 2,650, respectively. The proposed approach demonstrates strong performance in building localization and damage classification, providing a scalable solution for multi-source disaster assessment and recovery planning.**

Index Terms—**Building damage assessment; deep learning; dual-input triplet attention; multi-source remote sensing data; spatial pyramid pooling**

INTRODUCTION

Building damage assessment plays a critical role in post-disaster emergency response and reconstruction planning [1]. Remote sensing technology, combined with deep learning, enables rapid and automated evaluation of large-scale damage areas with high spatial and temporal efficiency [2],[3],[4]. In the field of post-disaster building damage assessment, early approaches primarily relied on manual evaluation based on expert experience and on-site surveys. With the advancement of remote sensing technology, methods leveraging synthetic aperture radar (SAR), interferometric SAR (InSAR) [5],[6],[7],[[8] and machine learning [9] have emerged. SAR and InSAR techniques have been widely applied in post-disaster assessment due to their sensitivity to surface changes and capability of providing information under different observation conditions. However, these approaches mainly focus on detecting physical changes or deformation patterns and may face challenges in directly identifying building-level damage categories. Yu et al. [10] integrated multi-class damage detection (MCDD) with random forest algorithms to assess building damage from multiple remote sensing data sources. In recent years, deep learning has been increasingly adopted for building damage assessment. The release of the xBD dataset has further promoted the development of deep learning-based building damage assessment by providing large-scale multi-disaster building annotations. Several studies have explored CNN-based, attention-based, and transformer-based approaches on this benchmark to improve building localization and damage classification performance. However, most existing xBD-based studies focus primarily on benchmark performance improvement, while the challenges of applying these models to real storm-induced disasters, integrating multi-source remote sensing information, and supporting regional-scale emergency assessment remain insufficiently explored [11],[12]. Weber et al. [13] treated building damage assessment as a semantic segmentation task, assigning different classes to varying damage levels.

Deep learning-based approaches can generally be categorized into those that utilize only post-disaster imagery and those that leverage both pre- and post-disaster images. Ci et al. [14] treated building damage assessment following the 2014 Ludian earthquake as a multi-classification problem, training a CNN on post-disaster images. Gupta et al. [15] proposed the RescueNet

[1] Institute of Remote Sensing and Geosciences, Hangzhou Normal University, Hangzhou 311121, China.

[2] Zhejiang Provincial Key Laboratory of Wetland Intelligent Monitoring and Ecological Restoration, Hangzhou 311121, China.

[3] University of Illinois Urbana-Champaign, Illinois State Water Survey, 2204 Griffith Dr, Champaign, IL 61820.

[4] College of Urban and Environmental Sciences, Peking University, Beijing 100871, China.

Corresponding author: Jiayi Fang E-mail: jyfang@hznu.edu.cn

framework, which models feature differences between pre- and post-disaster images using a dual-branch architecture. This process aligns closely with change detection techniques [16], which aim to identify pixel-level differences [17],[18],[19],[20].

Notably, existing research has achieved substantial progress in earthquake damage assessment [21],[22]. For instance, Xu et al. [23] proposed a large-scale vision model based on Transformer architecture, enabling universal segmentation of structural damage across multiple disaster types. Wang et al. [24] developed a geometry consistency-enhanced convolutional encoder-decoder framework using UAV imagery, achieving highly accurate and automated urban seismic damage assessment. These studies demonstrate that deep learning methods possess strong end-to-end learning capabilities and adaptability in complex structural damage scenarios. In comparison, storm-related meteorological disasters often cause more diverse and heterogeneous damage patterns to buildings. Unlike earthquake-induced damage, which is often characterized by structural failure patterns, storm-related disasters may generate more heterogeneous damage signatures, including roof damage, flooding-induced impacts, wind-related deformation, and debris effects. Furthermore, the spectral and geometric characteristics of storm-related damage are less distinct [25],[26],[27].

These storm-specific characteristics introduce new challenges for existing building damage assessment frameworks, especially those relying on simplistic feature fusion or designed for more uniform disaster types like earthquakes. Therefore, developing models that can effectively capture subtle cross-temporal variations and diverse damage signatures is essential for improving generalization across different disaster scenarios. A critical challenge in pre- and post-disaster image pair modeling lies in effectively representing the spatial and semantic correspondence between time phases. Most current models employ dual-branch CNNs with simple fusion schemes [28],[29],[30]. For instance, Hao et al. [31] concatenated features from pre- and post-disaster images and fed them into a CNN-based framework. We reveal that the primary limitation of the current U-Net-based BDANet model is the absence of appropriate strategies for leveraging global scene category cues [32]. The challenges in semantic segmentation include obtaining more precise object boundaries and resolving misclassification of small objects, particularly addressing the issue where objects of the same category can exist across multiple spatial scales [33].

This study focuses on Derna, Libya, as a case area, where severe urban flooding was caused by Mediterranean Storm Daniel in September 2023. While most existing studies center around earthquake scenarios, this work addresses the research inadequacy in other disaster scenarios. Furthermore, many previous approaches have been confined to pixel-level classification, lacking object-level building delineation, which is essential for operational decision-making and emergency planning.

To bridge these gaps, we propose a storm-oriented building damage assessment framework based on an improved BDANet architecture, named NBDANet(New BDANet). The model introduces two core modifications: a Spatial Pyramid Pooling (SPP) module integrated into both encoder paths to enhance global multi-scale context understanding [34]; and a newly designed Dual-input Triplet Attention (DTA) module as our key innovation, which realizes effective cross-feature interaction between pre- and post-disaster imagery and enabling more accurate damage severity classification.

We use the xBD dataset [35] for model training and validation and apply the model to Derna using high-resolution GeoEye-1 imagery. The methodological framework consists of three stages: (1) building segmentation using U-Net, (2) damage classification using a dual-branch multi-scale CNN, and (3) post-processing and validation using Sentinel-derived indices Normalized Difference Built-up Index (NDBI) [36] and SAR-based Damage Proxy (DP) [37], to provide complementary evidence for the spatial consistency of the detected damage patterns. In addition, Global Human Settlement Layer (GHSL) population data are incorporated to estimate population exposure and prioritize rescue efforts. By integrating pixel-level prediction, building-level assessment, and region-level impact zoning, this approach offers a scalable and transferable framework for post-disaster analysis and contributes valuable insights for humanitarian response and data-driven recovery planning.

RESULTS

Description of Study Area

The port city of Derna, situated at the mouth of the Derna River in northeastern Libya, has long grappled with seasonal flooding issues. On September 10, 2023, Storm Daniel, a mid-latitude cyclone with hybrid tropical cyclone characteristics [38],[39], made landfall along the eastern Mediterranean coast of Libya. The storm dumped over 400 mm of rainfall (Fig. 1), an amount of precipitation both rare and intense. This extreme rainfall triggered devastating floods in northeastern Libya. Derna was severely affected; specifically, two aging and inadequately maintained dams succumbed to the pressure of the heavy downpour. The subsequent collapse of the dams unleashed catastrophic floods, leading to tens of thousands of deaths and disappearances [6]. Fig. 1 illustrates the locations of disaster events in the xBD dataset, along with the location of the case study area in this research, the urban area of Derna, Libya.

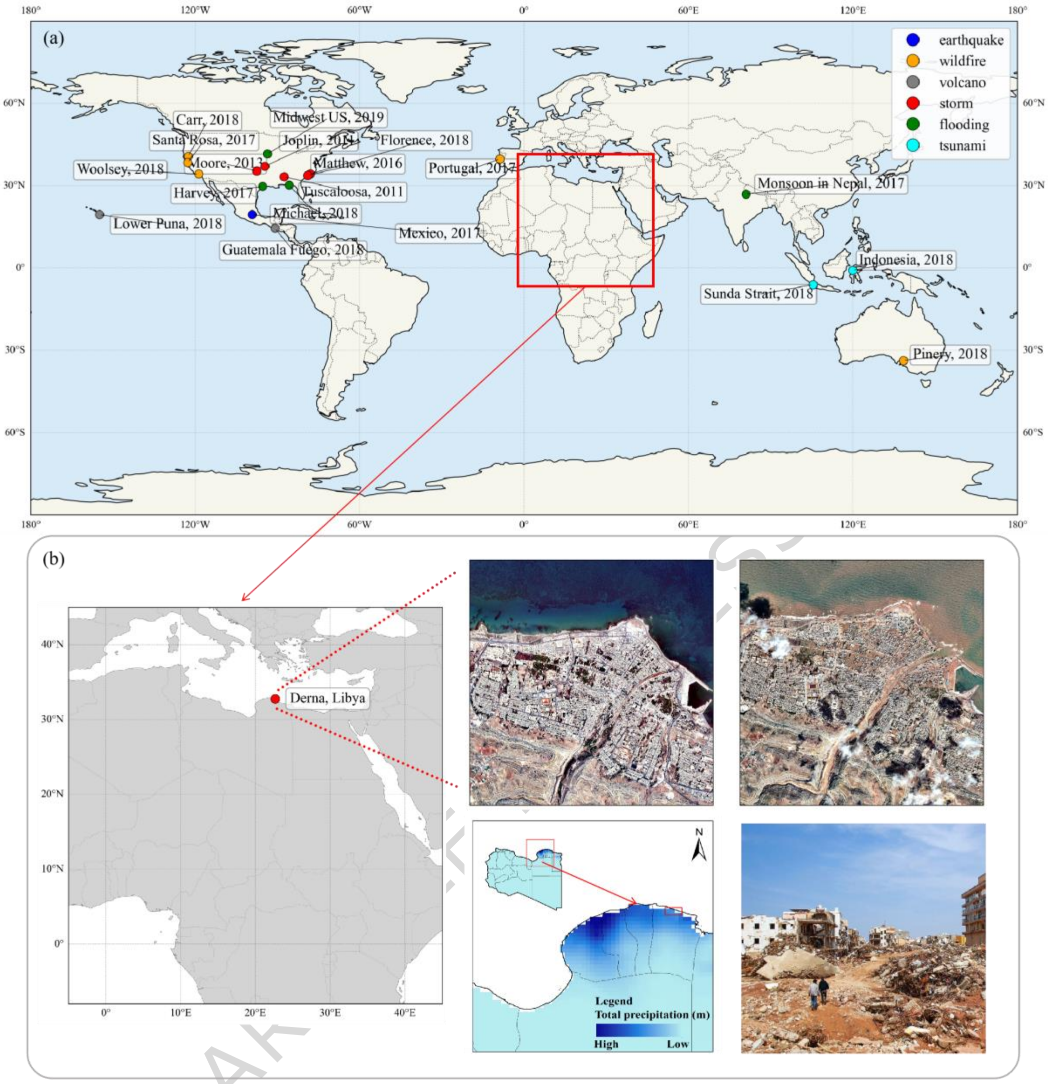

Fig. 1 The global scale study area for building damage assessment in sudden-onset disaster. (a) The global distribution of disaster events in the xBD dataset. (b) The disaster event locations, remote sensing imagery, and accumulated precipitation in this study.

Multi-source Remote Sensing Data

GeoEye-1 Remote Sensing Imagery: In this study, the optical remote sensing imagery of the study area before and after the disaster was obtained from the high-resolution commercial satellite GeoEye-1(Fig. 1). The imagery has a resolution of 0.41 m, with pre-disaster data acquired on July 1, 2023, and post-disaster data collected on September 13, 2023 (three days after the storm). High-resolution GeoEye-1 optical imagery was used to visualize the affected urban environment and provides detailed ground features necessary for accurately assessing building conditions [4].

Model Training and Testing Dataset: In this study, the xBD dataset [15] is used for the training and testing data. The xBD dataset is currently the only publicly available large-scale satellite image dataset for building damage assessment. It includes samples from 19 distinct disaster events (e.g., earthquakes, fires, volcanoes, storms, flooding, and tsunamis) , which enables the model to learn generalized damage representations across different hazard scenarios. Each image measures 1024×1024 pixels and comprises three RGB bands with a spatial resolution of up to 0.8 m [32]. The dataset provides high-resolution global image pairs of buildings before and after disasters, along with their labels. Based on raw data, where disaster-induced building damage levels had been professionally assessed and categorized into four levels, the detailed situation is shown in TABLE 1. The training set contains18,336 images with 632,228 building polygons. There are 313,033, 36,860, 29,904, and 31,560 building instances, respectively, for the *No damage*, *Minor damage*, *Major damage*, and *Destroyed*. This research fully adopted the established classification standard in its methodology. Among the four damage levels, *No damage* samples account for the majority (76.04%), while *Minor damage*, *Major damage* and *Destroyed* represent 8.98%, 7.29% and 7.69% respectively. Notably, the dataset exhibits significant class imbalance, with undamaged samples constituting 76.04% of the total. Therefore, in the data preprocessing process, the CutMix [61] technology is adopted.

TABLE 1
Damage Scale Description of xBD Dataset

Damage level	Visual Description of the Structure
No damage	Undisturbed. No sign of water, structural damage,shingle damage, or burn marks.
Minor damage	Building partially burnt, water surrounding the structure, volcanic flow nearby, roof elements missing, or visible cracks.
Major damage	Partial wall or roof collapse, encroaching volcanic flow, or the structure is surrounded by water or mud.
Destroyed	Structure is scorched, completely collapsed,partially or completely covered with water or mud,or no longer present.

Sentinel Series Data: The Sentinel series satellites are a key component of the Copernicus program of the European Space Agency (ESA) [40], plays a pivotal role in disaster monitoring [41],[42],[43]. Sentinel-1 operates a C-band Synthetic Aperture Radar (SAR) capable of acquiring Interferometric Wide Swath (IW) data, while the Multispectral Imager of Sentinel-2 provides comprehensive coverage across the visible to short-wave infrared spectrum [44],[45]. For this study, Sentinel-1 C-band SAR data and Sentinel-2 optical imagery were utilized to derive DP maps and NDBI, respectively. The DP calculation leveraged coherence differences between pre-disaster (August 19 and August 31, 2023) and post-disaster (September 12, 2023) ascending track (Path 102) SAR acquisitions. To mitigate geometric decorrelation effects, imagery pairs were selected with spatial baselines maintained below 150 m [46]. Sentinel-2 imagery acquired on September 7 2023 (pre-event) and September 22 2023 (post-event) over Derna city provided the optical data foundation. Specifically, Short-Wave Infrared (SWIR, band 11, 20 m resolution) and Near-Infrared (NIR, band 8, 10 m resolution) bands were used to compute NDBI [47]. Both DP and NDBI can indicate potential building damage through continuous spectral and coherence changes, but they cannot directly provide discrete damage level classification.

Population Data: This study uses the GHSL data to assess the impact on the population. The GHSL population data used in this study is the 2020 version, which is the most recent publicly available dataset closest to the time of the disaster. As this dataset primarily provides spatial population density reference, its static nature means that the short-term temporal gap has a limited impact on the estimation of the affected population. The GHSL population data is a dataset provided by the European Space Agency (ESA)-led Global Human Settlement Monitoring project [48]. The dataset has a resolution of 100 m and aims to provide global population information to support applications in disaster risk management, and other fields. The generation of the GHSL population data combines satellite imagery with statistical population data, using a model to estimate population distribution, and is provided in raster format. This study selected the 2020 population data of Libya, cropped it to obtain population raster data for the study area, and analyzed the affected population based on the building damage results.

Performance Evaluation on the xBD Dataset

Model training was conducted using the PyTorch framework in PyCharm, leveraging a single NVIDIA RTX 4090 GPU. Study area imagery was cropped to 1024×1024 pixels, with training inputs further reduced to 512×512 pixels while retaining full resolution (1024×1024) for testing. Data augmentation included standard transformations (flipping, scaling, rotation). Consistent convolutional block sizes and channel counts were maintained across segmentation and damage assessment tasks. The loss function combined cross-entropy and Dice loss. Training utilized SGD and Adam optimizers with learning rates of 1.5×10^{-4} (100 epochs) for segmentation and 2.0×10^{-4} (100 epochs) for damage grading.

To evaluate the effectiveness and generalization ability of the proposed NBDANet model, we conducted quantitative and qualitative comparisons on the xBD test set. Two sets of experiments were performed: benchmark comparisons against representative state-of-the-art models for building damage assessment, and ablation studies on core components of the proposed architecture.

TABLE 2 summarizes the overall F1 score ($F1_{overall}$), building localization accuracy ($F1_{loc}$), and damage classification accuracy ($F1_{dam}$) across seven models, including Siamese-UNet, MaskRCNN, ChangeOS variants [49], DamFormer [50], BDANet, BDANet variants [51],[52]and the proposed NBDANet. NBDANet achieved the highest overall performance, with an $F1_{overall}$ of 79.38%, $F1_{loc}$ of 86.93%, and $F1_{dam}$ of 76.15%, outperforming the original BDANet model and other state-of-the-art baselines. It fully demonstrates the improvement of the model's discriminatory ability in identifying buildings with damage levels. The overall xView2 metric can be computed by the weighted sum of the localization score and damage classification score, as follows:

$$F_1^{overall} = 0.3F_1^{loc} + 0.7F_1^{dam} \quad (1)$$

TABLE 2
Building damage assessment results on xBD dataset with different methods. All indicators are reported in percent (%).

Method	F1(overall)	F1loc	F1dam	No Dam	Minor Dam	Major Dam	Destroyed
Siamese-UNet	71.68	85.92	65.58	86.74	50.02	64.43	71.68
MaskRCNN	74.10	83.60	70.02	90.60	49.30	72.20	83.70
ChangeOS-34-PPS	77.52	85.16	74.25	92.19	58.07	72.84	82.79
ChangeOS-50-PPS	78.57	85.41	75.64	92.66	60.14	74.18	83.45
ChangeOS-101-PPS	78.52	85.69	75.44	92.81	59.38	74.65	83.29
DamFormer	77.02	86.86	72.81	89.86	56.78	72.56	80.51
BDANet	77.57	86.69	73.66	95.46	57.59	68.84	83.78
Net + HAAM	77.75	86.51	73.72	95.38	57.70	69.32	82.84
Net + FACMA	77.01	86.92	72.75	93.73	51.97	74.64	84.63
NBDANet	79.38	86.93	76.15	94.19	58.72	76.66	84.47

To assess the contribution of the proposed modules—SPP and DTA—an ablation study was conducted, as presented TABLE 3. The "Vanilla" model refers to the original BDANet baseline without either SPP or DTA. Adding SPP alone led to an improvement in overall F1 score from 77.57% to 78.04%, mainly enhancing the *Major damage* category. Introducing DTA alone improved $F1_{dam}$ from 73.66% to 74.80%, demonstrating the benefit of cross-temporal feature interaction. The SPP and DTA modules were selected after exploring several alternative architectural modifications. Other candidate modules either provided negligible accuracy improvements or substantially increased computational complexity. The classification confusion matrix of proposed framework is reported in TABLE 4. The full configuration (NBDANet) that integrates both SPP and DTA achieved the best results in all key metrics, verifying the complementary advantages of the two modules.

TABLE 3
Ablation study of different components (SPP and DTA strategy) in the proposed framework. All indicators are reported in percent (%).

Method	F1(overall)	F1loc	F1dam	No Dam	Minor Dam	Major Dam	Destroyed
Vanilla	77.57	86.69	73.66	95.46	57.59	68.84	83.78
Vanilla + SPP	78.04	86.93	74.23	93.84	55.09	75.11	84.99
Vanilla + DTA	78.37	86.69	74.80	95.93	60.15	69.40	83.23
NBDANet	79.38	86.93	76.15	94.19	58.72	76.66	84.47

Qualitative comparison results are shown in Fig. 2. Both BDANet and NBDANet results are presented alongside the ground truth. As shown, NBDANet yields better delineation of building contours and more accurate damage classification, particularly in high-severity cases. It also exhibits improved alignment with ground truth at the instance level, supporting its practical utility in operational damage assessment. In addition, the last column of Fig. 2 illustrates the building-level results, which are derived from pixel-wise outputs of the model. Specifically, we aggregated pixel-level predictions into individual building instances using a weighted formula, thereby enabling a more intuitive representation of building-scale damage assessment, providing an object-oriented representation for practical disaster assessment.

TABLE 4
Classification confusion matrix (%) of proposed NBDANet on xBD testing set.

Damage Level	(C1)	(C2)	(C3)	(C4)
No damage (C1)	95.9	3.1	0.6	0.4
Minor Damage (C2)	24.4	64.1	9.9	1.6
Major Damage (C3)	9.8	8.5	78.2	3.5
Destroyed (C4)	2.1	3.6	9.1	85.2

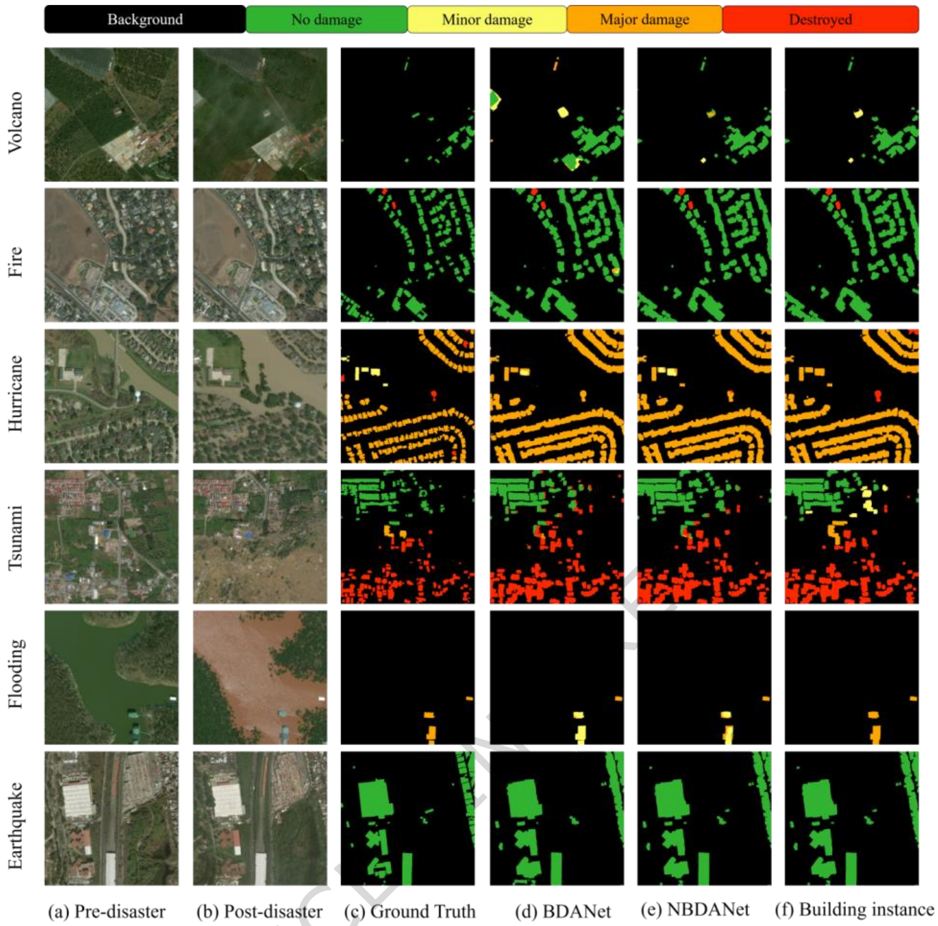

Fig. 2. Qualitative comparison results on representative samples from the xBD dataset, covering multiple disaster types. These examples are used to demonstrate the general performance of the model. (a) pre-disaster, (b) post-disaster, (c) ground truth, (d) BDANet, (e) NBDANet, (f) Building instance (individual building).

Building Damage Assessment and Damage Severity Zoning

The trained model processes pre- and post-disaster imagery to identify building locations and classify damage severity. In the first stage of building localization, the model outputs a building probability map (P_{loc}). To refine segmentation outputs, we evaluated the segmentation performance under different threshold values using the IoU metric. All thresholds are configured within the range of 0–255. Fig. 3 illustrates the Intersection over Union IoU variation curve corresponding to different thresholds. The experimental results indicate that a threshold of 62 achieves the best balance between eliminating false detections and preserving true building boundaries. In the second stage, the model generates four damage-level probability maps based on the first-stage output. Probability maps are selected according to the highest confidence scores to classify individual pixels into corresponding damage categories. To reduce classification noise, predicted results are upscaled to match the original image resolution. Then, the area of each connected domain is calculated. By progressively testing different values (e.g., 35, 45, 55, 65) and evaluating their impact on the results, we found that a threshold of 55 pixels achieved a favorable balance between suppressing noise and retaining valid building areas , so the patches with less than 55 pixels are removed. This study also constructed a 7×7 square corrosion core to apply image erosion, separating connected buildings [62]. These operations are lightweight and do not alter the overall spatial patterns, but mainly serve to reduce noise and improve visual and structural consistency. Optimized building masks are derived through morphological operations, produce final damage assessment maps (Fig. 4). Fig. 4 presents pre- and post-disaster image pairs (a-b), initial segmentation results (c), and optimized outcomes (d). Close-up views (Fig. 4e-h) reveal that initial segmentation misclassified non-building regions (e.g., roadside plots) and produced merged building footprints. Post-processing effectively removes low-probability pixels (roads, vegetation, bare soil) while sharpening building boundaries, significantly improving localization accuracy.

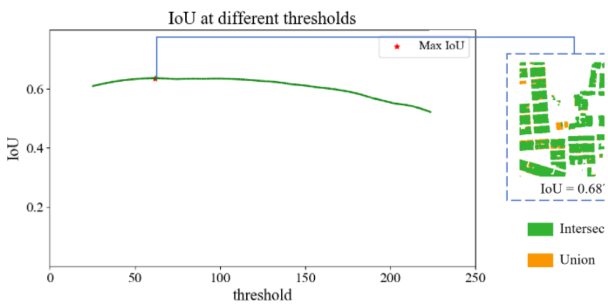

Fig. 3. Pixel-level building localization performance under different segmentation thresholds.

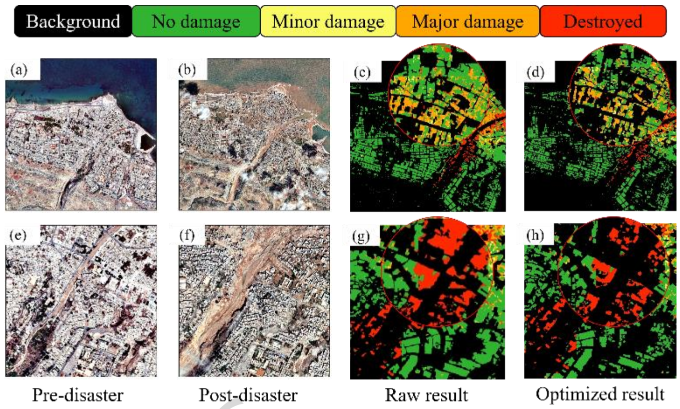

Fig. 4. Comparison between raw and optimized results. The first and second columns show the pre- and post-disaster images. The third column shows the raw results from BDANet. The fourth column shows the optimized results. (a-d) Large-scale images and results, (e-h) Small-scale images and results.

Based on the optimized results, TABLE 5 shows the distribution of areas with varying damage levels within the study area of Derna City (Fig. 5). Severely damaged buildings have either collapsed or sustained structural damage. It shows 21.74% of the buildings in the study area suffered damage to varying levels, with *Major damage* and *Destroyed* buildings accounting for 20%. These data provide a foundation for further exploration of building damage conditions.

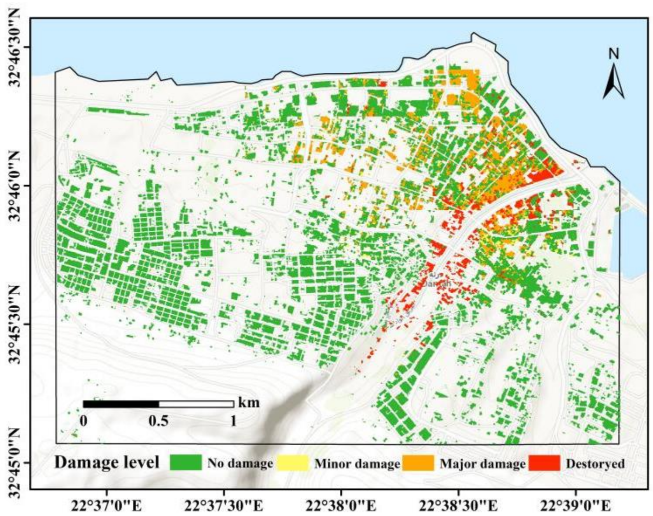

Fig. 5. Building damage assessment results.

TABLE 5
BUILDING AREA WITH DIFFERENT DAMAGE LEVELS

	No	Minor	Major	Destroyed

	damage	damage	damage	
No.of cells(10^3)	17319.1	462.4	2839.3	1509.6
Area (km^2)	1.61	0.04	0.26	0.14
Proportion	78.26%	2.09%	12.83%	6.82%

Following optimization of building damage results, individual building damage assessment was conducted for the Derna area. Building damage level were computed using Formula (5), with results visualized in Fig. 6. Affected areas are primarily concentrated along river corridors and coastal plains in the city center. These regions exhibit high building density and lie within the main flood impact zone, leading to more severe damage. Significant spatial transitions occur between damage severity levels, with lightly damaged areas mostly distributed on the periphery of severely damaged areas. Compared to the segmentation results presented in Fig. 5, this assessment provides a more intuitive visualization of damage severity distribution.

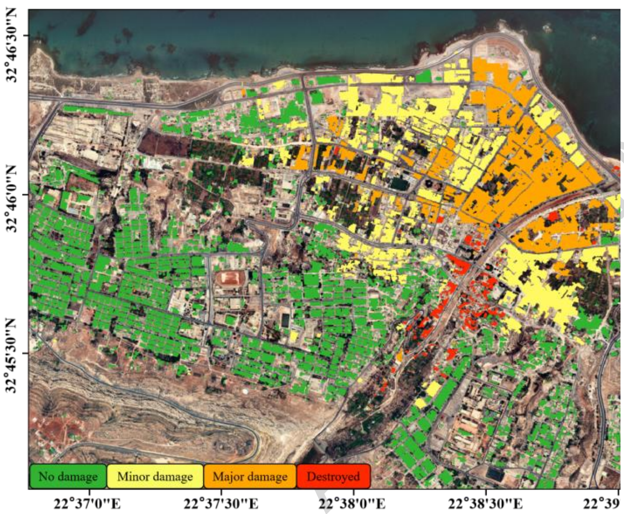

Fig. 6. Individual building damage assessment.

Building damage assessment processes inherently contain certain limitations. Firstly, partial pixel damage within a building may result in over-classification to higher severity levels. This discrepancy arises from uneven damage distribution across building footprints and inherent limitations of the classification algorithm. Secondly, irregular building outlines or spectral similarity to surrounding features may lead to misclassification of boundary pixels, further compromising damage level accuracy. The research can optimize classification algorithms to account for intra-building damage heterogeneity and incorporating fine-grained geometric features to improve boundary delineation.

To enhance support for disaster management and rescue planning, damage severity zoning was performed based on building damage assessment results [53]. Leveraging the sub-meter spatial resolution of original imagery and detailed building damage information, assessment outputs were resampled to 50 m resolution for zoning purposes. The 50m resolution balances detail retention with computational efficiency, ensuring practical applicability in emergency response scenarios. The study area was classified into four damage categories: *No damage*, *Minor damage*, *Major damage*, and *Destroyed* (Fig. 7). This zoning approach effectively communicates the spatial distribution of affected areas while providing a scientific basis for formulating tailored rescue and reconstruction strategies.

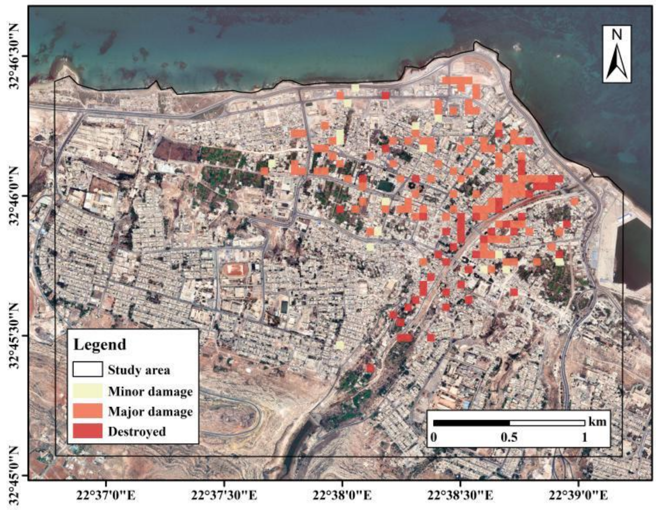

Fig. 7. Damage severity zoning (Based on building damage results).

Complementary Validation with DP and NDBI

Due to the lack of publicly available comprehensive building damage annotations for the Derna event, quantitative pixel-level validation was not feasible. Therefore, the reliability of the results was assessed using multi-source remote sensing indicators and building footprint comparisons. This study combines the NDBI with the DP map to perform collaborative validation with the building damage classification map. NDBI effectively identifies damaged building areas by comparing reflectance differences [10]. Since SAR data is not affected by weather conditions and diurnal variations, DP can penetrate cloud cover, which is common during floods, effectively complementing the blind spots of optical data.

Based on Sentinel-2 Short-Wave Infrared (SWIR, Band 11) and Near-Infrared (NIR, Band 8) data, the mean difference in NDBI values before and after the disaster (ΔNDBI) is calculated [36]. The results (Fig. 8a) show that the severely damaged building areas in Derna city are distributed in a strip along the river, highly consistent with the main flood path. For example, the downstream of the river, where the dam breach caused severe damage, shows NDBI values generally above 0.8, reflecting the collapse of surface structures and the destruction of building clusters. Based on the Sentinel-1 ascending C-band SAR data, the Maximum Likelihood Coherence (γ_{MLC}) is calculated using GMTSAR software. The $\Delta\gamma$ is normalized to the range [0,1], with higher $\Delta\gamma$ values indicating more severe damage. The final DP is generated through 10 m resolution resampling (Fig. 8b). The results show that the spatial distribution characteristics of NDBI, DP, and the deep learning model results are significantly correlated. Image comparison (Fig. 8c) reveals that high-value NDBI and DP areas highly overlap with the areas classified as *Destroyed* by the model (Fig. 5). The areas classified by the model as *Minor Damage* exhibit moderate NDBI values, while DP map values are generally below 0.4, which may be associated with localized surface erosion or water accumulation, but did not cause large-scale structural collapse. High-resolution GeoEye-1 imagery shows that the building forms in these areas remain largely intact, validating the classification rationality of multi-source remote sensing results. Consistency checks across the three methods further demonstrate their complementary strengths. These approaches provide comprehensive characterization of building damage extent in the study area.

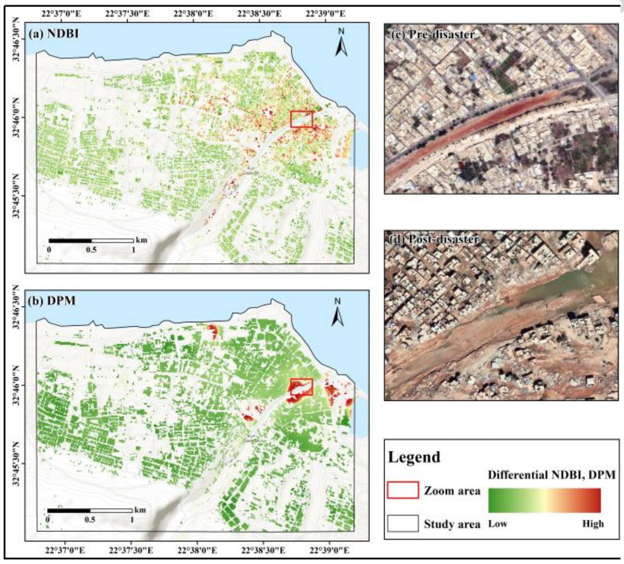

Fig. 8. NDBI and DP map building damage assessment results. (a) NBDI, (b) DP map, (c) Pre-disaster image, (d) Post-disaster image.

It is worth noting that, although we visually observe a clear spatial consistency between areas classified as *Destroyed* by the model and high-value regions in the NDBI and DP maps, both NDBI and DP are continuous indices ranging from 0 to 1. Currently, there is no standardized classification scheme to map these values directly to specific damage levels, it is difficult to establish explicit quantitative overlap analysis. Therefore, in this study, we adopt visual comparison as a means to illustrate spatial trend consistency, serving as an auxiliary validation approach to enhance the interpretability of the model outputs and their logical coherence with multi-source data, rather than as a basis for performance evaluation.

Calculation of Affected Population

Given the strong correlation between damaged building distribution and affected population, this study analyzed disaster impacts using GHSL population datasets. This study selected the 2020 population data of Libya, cropped it to obtain population raster data for the study area, and analyzed the affected population based on the building damage zoning results. Analysis results presented in TABLE 6 indicate approximately 5,200 residents occupy *Major damage* areas and 2,650 inhabit *Destroyed* areas. Population distribution patterns reveal residents of Derna primarily concentrated along riverbanks and coastal plains. As Fig. 7 demonstrates, riverside dwellings incurred the most severe flood damage, affecting large population clusters. While building and population distributions generally align, discrepancies highlight areas requiring targeted emergency response. This spatial analysis identifies high-density zones with severe damage, prioritizing these regions for urgent rescue and recovery efforts.

TABLE 6
THE NUMBER OF PEOPLE AFFECTED BY DIFFERENT LEVELS OF DAMAGE

	No damage	Minor damage	Major damage	Destroyed
Population	26861	693	5214	2654
Proportion	75.83%	1.96%	14.72%	7.49%

To enhance disaster response accuracy, this study analyzed the damage classification map and population distribution map in conjunction [54]. Given the 100 m resolution of population data, uncertainties exist in estimating affected populations. To address this, results were resampled to quantify social impacts of building damage. Building pixel counts corresponding to each population raster cell were calculated, then categorized into three levels alongside population density values. This process generated a binary gradient statistical map (Fig. 9), where cells aligned diagonally with the legend represent congruent building pixel-population density relationships. This visualization identifies zones with severe building damage and high population density, prioritizing these areas for targeted rescue efforts due to their elevated risk of casualties.

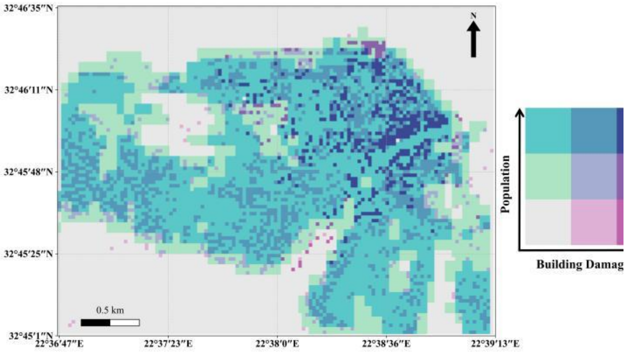

Fig. 9. Bivariate graduated statistical chart of the distribution of building and population.

DISCUSSION

Building extraction from high-resolution remote sensing imagery remains a challenging task due to diverse image patterns and large spatial scales. To address these limitations, this study proposes a redesigned architecture—NBDANet, evolved from the original BDANet model—featuring a two-stage framework with integrated enhancements. In both stages, a SPP module is embedded at the bottom of the encoder to strengthen multi-scale feature extraction. This enhancement is achieved with minimal computational overhead, ensuring that the model maintains a favorable trade-off between performance and efficiency. To further improve damage classification, this study introduces the DTA module into the second stage. Unlike conventional attention mechanisms, DTA performs bidirectional attention exchange across spatial dimensions between pre- and post-disaster image features. This cross-temporal interaction enhances the model's ability to detect subtle differences, particularly for moderate and severe damage levels. As shown in the ablation study (TABLE 3), the inclusion of DTA led to consistent gains in classification performance across all severity categories.

To further improve building boundary delineation, this study combines thresholding to exclude low-confidence building areas with morphological erosion to remove noise. The NBDANet model achieved successful cross-regional transfer to the Derna area for building damage assessment, thereby demonstrating its generalizability for high-resolution imagery. This approach effectively mitigates issues arising from insufficient training samples and significantly reduces total processing time from data preparation to prediction.

To validate the accuracy of building location information, actual building data were collected and analyzed using stratified random sampling. The building data were obtained from OpenStreetMap, which provides publicly accessible and widely used geographic information. Three representative zones in Derna were selected for verification: a high-rise building zone (a), a suburban region (b), and a densely populated residential area (c). Verification results are presented in Fig. 10. The validation process achieved an average accuracy of 79.5% across the three zones, with a recall rate of 86.8% for sampled buildings. Strong segmentation performance reflected the real-world distribution of buildings in Derna.

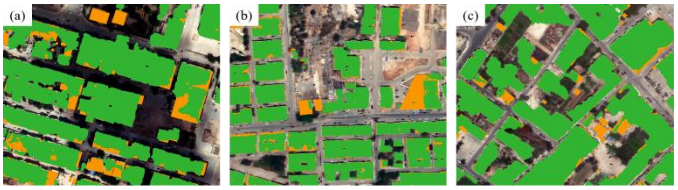

Fig. 10. Visual interpretation intersects the prediction of the model, where green represents true positive (TP) and yellow represents false negative (FN).

Although the model trained in this study performs well in the Derna region, we acknowledge that when applied to new scenarios with significant differences in building structure, materials, or imaging conditions, the model may face generalization challenges. In the future, integrating few-shot learning into remote sensing-based building damage assessment frameworks could be particularly valuable for rapid disaster response tasks characterized by sudden events and scarce labels, exploring the fusion mechanisms between multi-source remote sensing data and few-shot learning.

In deep learning-based building damage assessment, initial damaged area identification is formulated as an image segmentation task. However, maintaining intact boundaries of damaged buildings remains challenging. This study enhances the damage assessment accuracy in the second processing stage by incorporating building localization results from the first stage. The specific context of this research involves flood erosion triggered by dam breaches. High-velocity floodwaters alter surface features, creating dynamic environmental conditions that may impede model identification and classification processes. These alterations introduce uncertainty into building damage assessment results due to the complex interactions between flood dynamics and urban infrastructure.

Despite the overall effectiveness of the proposed framework, several sources of error may influence the classification results. First, data-related factors such as class imbalance in the xBD dataset and potential subjectivity in labeling, especially between adjacent categories (e.g., Minor and Major damage), introduce uncertainty. Second, the model is more sensitive to severe structural changes, while subtle damage patterns are harder to distinguish due to weak spectral and spatial variations. Finally, the aggregation from pixel-level predictions to building-level classification, along with post-processing operations, may amplify local misclassifications. These factors should be considered when interpreting the results.

Due to the lack of ground-truth damage data. To validate research result reliability, multi-source remote sensing data were used for cross-validation. Combined analysis of Differential NDBI derived from Sentinel-2 and DP generated from Sentinel-1 demonstrates spatial coincidence between model-identified severe damage zones (Fig. 5) and regions exhibiting significant declines in optical spectral characteristics and radar coherence. However, DP has inherent limitations. For instance, flood erosion leading to lose sediment cover reduces coherence significantly. As Fig. 5 illustrates, the model classifies these areas as *No damage* or *Minor damage* consistent with both NDBI results and ground observations. The multi-source remote sensing data used in this study were acquired as close as possible to the time of the disaster, in order to minimize assessment errors caused by temporal discrepancies.

This study also identifies limitations in the existing data chain, such as the GHSL 2020 dataset lacking seasonal population mobility information. This deficiency results in underestimation of affected populations in coastal resort areas, where actual numbers were approximately 40% higher than estimates based on the 2023 Quarterly Tourism Report released by Derna Tourism Bureau (DMO, 2023). Although population data resampling introduces certain uncertainties, this method provides a reference framework for short-term decision-making in disaster response scenarios. Future research directions include integrating real-time dynamic data to improve assessment accuracy.

METHODS

The Proposed NBDANet Architecture and Module Improvements

Building damage assessment typically involves three conceptual phases: object detection, semantic segmentation, and damage severity grading, which form a general pipeline commonly adopted in the field [55]. This study proposes an improved deep learning framework—NBDANet—developed based on the original BDANet model [32], which takes pre- and post-disaster satellite imagery as dual inputs. To validate the performance of the model, Sentinel-1 SAR and Sentinel-2 optical data were integrated to derive the NDBI [36] and DP [37], respectively. The methodological framework of this study is systematically illustrated in Fig. 11.

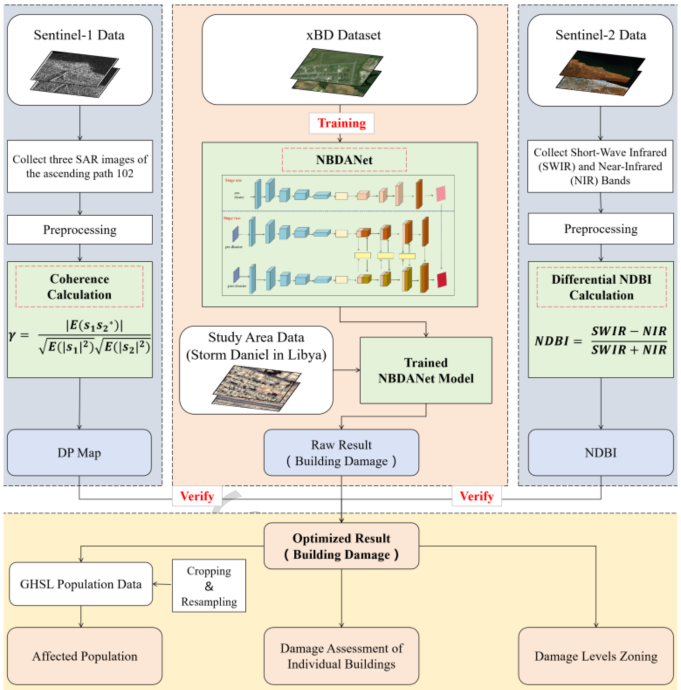

Fig. 11. Workflow of building damage assessment by storm flood.

This study builds upon the original BDANet framework and proposes an enhanced deep learning model named NBDANet, specifically designed for building damage assessment under storm-induced disaster scenarios. The improved NBDANet adopts a sequential two-stage architecture (Fig. 12). In both stages, Spatial Pyramid Pooling (SPP) modules are inserted at the bottom of the encoder to improves global contextual representation for building segmentation. SPP and related multi-scale context aggregation methods (e.g., PSPNet) have been widely adopted in semantic segmentation. The first stage performs pre-disaster building localization, while the second stage focuses on damage level classification through the fusion of pre- and post-disaster image features.

In the first stage, a U-Net-based encoder-decoder structure is used, with ResNet50 as the backbone to extract hierarchical features from pre-disaster imagery [56]. The encoder processes input data through a series of residual blocks (layer1-1 to layer1-5), utilizing 3×3 convolutions, batch normalization, and ReLU activation to generate deep features. Skip connections [56] between residual blocks preserve low-level spatial details and mitigate gradient degradation. To address the limited global receptive field of the encoder [57], a SPP module [33] is introduced after the encoder (Fig. 12b). The module employs adaptive average pooling with kernel sizes of 1×1, 2×2, 3×3, and 6×6 to capture multi-scale spatial features, which are then concatenated and compressed via 1×1 convolutions for dimensionality reduction [58]. This enhances the encoder's global contextual awareness and improves building boundary recovery during decoding [34]. The decoder uses transposed convolutions and skip connections to generate final building probability masks at the original resolution. The output of the first stage is a probability map, denoted as $P_{loc} \in R^{2\times H\times W}$, where H and W represent the height and width, respectively. The first channel represents the probability of the background and the second channel represents the probability of the building. Quantitative evaluation of the effectiveness of the SPP module was conducted using F1 score [59], with performance metrics calculated as follows:

$$\mathrm{Precision} = \frac{\mathrm{TP}}{\mathrm{TP+FP}} \tag{2}$$

$$\mathrm{Recall} = \frac{\mathrm{TP}}{\mathrm{TP+FN}} \tag{3}$$

$$\mathrm{F1} = \frac{2\times\mathrm{Precision}\times\mathrm{Recall}}{\mathrm{Precision+Recall}}. \tag{4}$$

where TP represents true positives, FP represents false positives, and FN represents false negatives.

In the second stage, both pre- and post-disaster images are input simultaneously. The encoder retains the SPP module to enrich multi-scale feature learning, and a Multi-scale Feature Fusion (MFF) module is employed to aggregate features across multiple resolutions (1× and 0.5× input scale) [60]. To support effective cross-temporal feature integration, this study proposes an improved attention module, named Dual-input Triplet Attention (DTA) (Fig. 12c), to replace the original CDA module, which is adapted from the original Triplet Attention mechanism. Unlike the original single-input design, DTA is structured as a dual-input, dual-output attention module, specifically tailored for disaster-related change detection tasks. It facilitates effective interaction between pre-disaster and post-disaster features across three dimensions—height, width, and spatial domain—thereby enhancing temporal feature fusion and improving coordination between localization and damage classification branches. The DTA module is specifically designed to model cross-temporal feature interactions, which are critical for distinguishing different levels of building damage. During data preprocessing, the CutMix technique [61] is implemented. This augmentation method involves randomly selecting two images, cutting and swapping portions of their content to generate synthetic training samples, alleviating sample imbalance, and thereby improving model generalization.

The final output is a probability tensor $P_L \in R^{5\times H\times W}$, with each channel encoding spatial likelihoods for building presence and four damage severity levels. Specifically, P_{L1} represents the building mask, and P_{L2} to P_{L5} represent *No damage*, *Minor damage*, *Major damage*, and *Destroyed*, respectively. To refine segmentation outputs, thresholding is applied to the building probability map using optimal IoU-based thresholds. The optimal threshold value for is determined using the following formula:

$$\mathrm{P_{thre}}(\mathrm{x},\mathrm{y}) = \begin{cases} 0 & \mathrm{P_{L1}}(\mathrm{x},\mathrm{y}) < \mathrm{threshold} \\ 1 & \mathrm{P_{L1}}(\mathrm{x},\mathrm{y}) \geq \mathrm{threshold} \end{cases} \tag{5}$$

where, x and y represent the horizontal and vertical coordinates of the cells respectively. The study employs the Intersection over Union (IoU) metric to evaluate the accuracy of results at different threshold values.

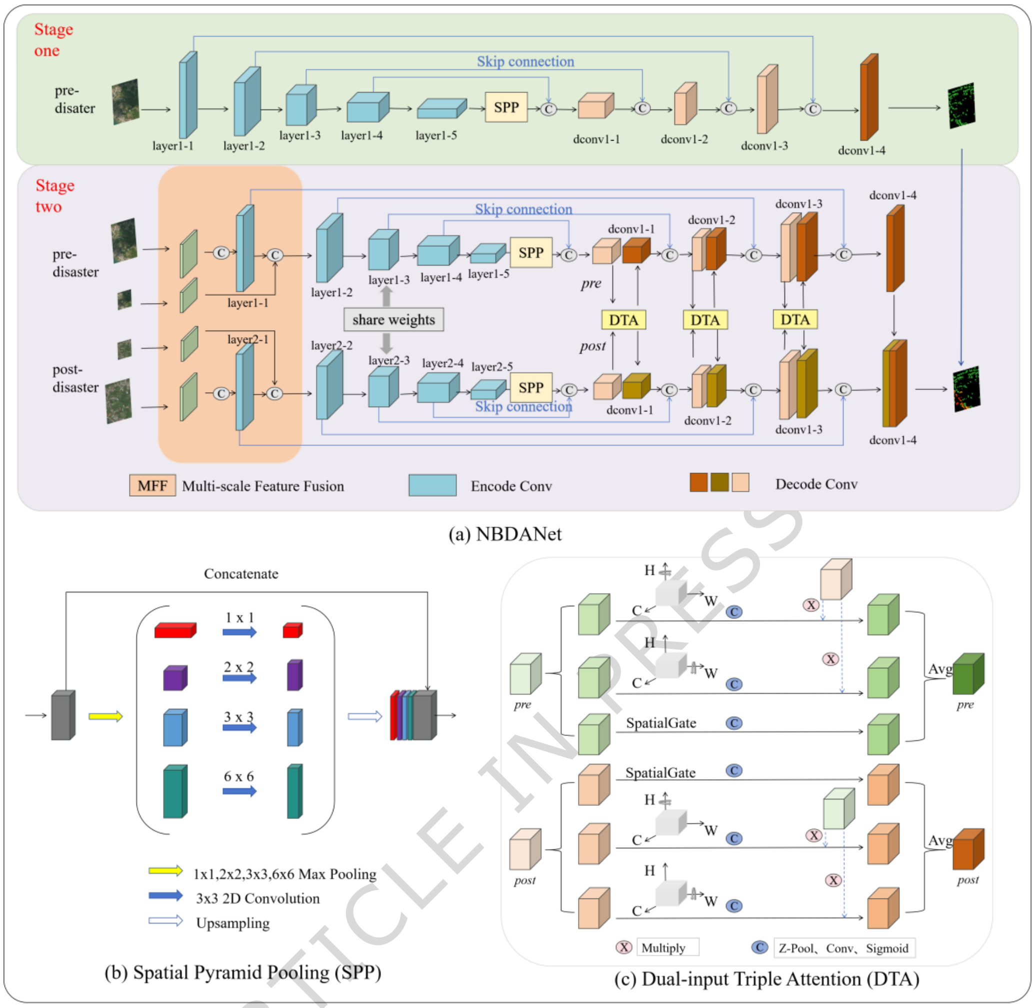

Fig. 12. Overview of the NBDANet framework. (a) The NBDANet, (b) spatial pyramid pooling module structure with four pooling scales, (c) dual-input triple attention (DTA) module.

Following post-processing, the binary building mask is element-wise multiplied with damage probability maps to suppress false classifications outside building regions. For each detected building footprint, pixel counts of the four damage classes are calculated, and a weighted scoring scheme is used to assign a final damage level [62]:

$$\text{Damage level} = \text{ceiling}\left(\frac{P_1+2P_2+3P_3+4P_4}{P_1+P_2+P_3+P_4}\right) \tag{6}$$

where P_1–P_4 are the pixel counts for the four damage levels. This allows individual building-level grading based on fine-grained, pixel-wise predictions, supporting downstream damage mapping and regional impact analysis.

Normalized Difference Built-up Index and Damage Proxy Map

NDBI plays an important role in extracting building information from remote sensing imagery [36]. By contrasting the reflectance differences between different bands, NDBI highlights the spectral differences between buildings and other land cover types such as vegetation and water bodies [63]. In disaster scenarios, the damage to buildings often leads to changes in physical structures and spectral characteristics, resulting in significant alterations in spectral reflectance. This study uses the characteristics of NDBI to capture the changes of buildings after disasters. Its calculation formula is:

$$\text{NDBI} = \frac{\text{SWIR}-\text{NIR}}{\text{SWIR}+\text{NIR}} \tag{7}$$

NDBI was calculated using the short-wave infrared (SWIR) and the near-infrared (NIR) bands. Before calculation, all bands were resampled to a 10 m pixel spacing to maintain consistency in spatial resolution across different bands. Additionally, the pixel digital values are converted to reflectance values ranging from 0 to 1 to eliminate numerical differences caused by the inherent characteristics of the sensor, and the outlier value is corrected [47].

This paper also applies one frame of three scenes along a single ascending Sentinel-1 path (Frame 175 in Path 102). Coherence, a byproduct derived during interferogram generation, quantifies the quality of the interferometry by measuring the similarity between two repeat-pass SAR signals in complex format [64],[65]. The precise definition is given by the equation:

$$\gamma = \frac{|E(s_1 s_2^*)|}{\sqrt{E(|s_1|^2)}\sqrt{E(|s_2|^2)}} \tag{8}$$

where s_1 and s_2 represent the SAR signals from two different dates. SAR coherence has been applied in flooding induced change detection frequently [66],[67],[68].

This study utilized the on-demand processing service provided by the Alaska Satellite Facility (ASF) to generated two interferograms using three SAR images from an ascending path 102, i.e., two SAR images before the flooding event and one after the event. We adopted the 10x2 looks to achieve 40 m pixel spacing in the SAR coherence products. The DP map was then derived from the differential coherence [69],[70], including the histogram matching to calibrate the post-flooding coherence map based on the probability density function (PDF) of the pre-flooding coherence, and applying causality constraint to adjust the negative values to be zeros to enhance the signal-to-noise ratio [65],[69]. The processed map is normalized to the range [0, 1] and resampled to a 10 m pixel spacing, generating the DP map. Higher DP indicates increased damage severity due to the flooding disaster.

Both DP and NDBI can detect building damage. NDBI derived from optical images has the advantage of rich spectral information and provides valuable insights into the variations in ground surface albedo associated with changes due to the strom disaster [71]. DP derived from SAR images can penetrate cloud cover and work all-day in all climate conditions [72]. By integrating NDBI and DP with deep learning models, the reliability of model evaluation results can be further enhanced, enabling a more accurate assessment of the extent and scope of building damage.

Data Availability: The xBD dataset used in this study is publicly available and can be accessed through official channels. The GeoEye-1 imagery and auxiliary remote sensing products analyzed during the current study are available from the corresponding author on reasonable request.

Code Availability: The code and implementation details used in this study are available from the corresponding author on reasonable request. The experiments were conducted using Python and PyTorch frameworks.

Acknowledgements: This research was supported by the National Natural Science Foundation of China (No. 42371078), the MOE (Ministry of Education in China) Liberal Arts and Social Sciences Foundation (No. 25YJCZH045), the Zhejiang Provincial Emergency Management Science and Technology Project (No. 2025YJ021), and the HZNU Scientific Research and Innovation Team Project (No. TD2025008).

Author Contributions: Conceptualization, Y.Y.and J.F.,methodology, Y.Y., X.Y validation, Y.Y, W.B., investigation, Y.Y., data curation, Y.Y. and W.B., writing-original draft preparation, Y.Y., writing-reviewand editing, Y.Y.and W.B., supervision, J.F, H.X.and X.H.,funding acquisition, J.F. and T.H. All authors have read and agreed to the published version of the manuscript.

Conflicts of Interest: The authors declare no competing financial or non-financial interests.

References

[1] Yamaguchi T, Mizutani T, Tarumi M, Su D. Sensitive damage detection of reinforced concrete bridge slab by "time-variant deconvolution" of SHF-band radar signal. IEEE Transactions on Geoscience and Remote Sensing. 2018; 57(3): 1478-1488.

[2] Kim J M, Son K, Kim Y J. Assessing regional typhoon risk of disaster management by clustering typhoon paths. Environment, Development and Sustainability. 2019; 21: 2083-2096.

[3] Al Shafian, Sultan, Hu D. Integrating machine learning and remote sensing in disaster management: A decadal review of post-disaster building damage assessment. Buildings. 2024; 14(8): 2344.

[4] Wang D, Du B, Zhang L. Adaptive spectral–spatial multiscale contextual feature extraction for hyperspectral image classification. IEEE Transactions on Geoscience and Remote Sensing, 2020; 59(3): 2461-2477.

[5] Ge P, Gokon H, Meguro K. A review on synthetic aperture radar-based building damage assessment in disasters. Remote Sensing of Environment. 2020; 240: 111693.

[6] Shirzaei M, Vahedifard F, Sadhasivam N. Aging dams, political instability, poor human decisions and climate change: recipe for human disaster. NPJ Natural Hazards. 2025; 2(1): 5.

[7] Normand J C L, Heggy E. Assessing flash flood erosion following storm Daniel in Libya. Nature Communications. 2024; 15(1): 6493.

[8] Serkhane A, Benfedda A, Guettouche M S. InSAR derived co-seismic deformation triggered by the Mihoub (Tell Atlas of Algeria) 28 May 2016 (Mw= 5.4) earthquake combined to geomorphic features analysis to identify the causative active fault. Journal of African Earth Sciences. 2022; 188: 104476.

[9] Guo Z, Shao X, Xu Y. Identification of village building via Google Earth images and supervised machine learning methods. Remote Sensing. 2016; 8(4): 271.

[10]Yu X, Hu X, Song Y. Intelligent assessment of building damage of 2023 Turkey-Syria Earthquake by multiple remote sensing approaches. NPJ Natural Hazards. 2024; 1(1): 3.

[11]Ji M, Liu L, Buchroithner M. Identifying collapsed buildings using post-earthquake satellite imagery and convolutional neural networks: A case study of the 2010 Haiti earthquake. Remote Sensing. 2018; 10(11): 1689.

[12]Wang N, Zhao X, Zhao P. Automatic damage detection of historic masonry buildings based on mobile deep learning. Automation in Construction. 2019; 103: 53-66.

[13]E Weber, H Kane. Building disaster damage assessment in satellite imagery with multi-temporal fusion. ArXiv Preprint ArXiv:2004.05525. 2020.

[14]Ci T, Liu Z, Wang Y. Assessment of the degree of building damage caused by disaster using convolutional neural networks in combination with ordinal regression. Remote Sensing. 2019; 11(23): 2858.

[15]Gupta R, Goodman B, Patel N. Creating xBD: A dataset for assessing building damage from satellite imagery. Proceedings of the IEEE/CVF Conference on Computer Vision and Pattern Recognition Workshops. 2019: 10-17.

[16]Tewkesbury A P, Comber A J, Tate N J. A critical synthesis of remotely sensed optical image change detection techniques. Remote Sensing of Environment. 2015; 160: 1-14.

[17]Wu L, Tong J, Wang Z. Post-flood disaster damaged houses classification based on dual-view image fusion and Concentration-Based Attention Module. Sustainable Cities and Society. 2024; 103: 105234.

[18]Ma H, Liu Y, Ren Y. Improved CNN classification method for groups of buildings damaged by earthquake, based on high resolution remote sensing images. Remote Sensing. 2020; 12(2): 260.

[19]Guan P, Lam E Y. Multistage dual-attention guided fusion network for hyperspectral pansharpening. IEEE Transactions on Geoscience and Remote Sensing. 2021; 60: 1-14.

[20]Lin Y, Hu X, Lu H. Multi-annual inventorying of retrogressive thaw slumps using domain adaptation. Journal of Geophysical Research: Machine Learning and Computation. 2025; 2(1): e2024JH000370.

[21]Wang Y, Jing X, Xu Y. Geometry-guided semantic segmentation for post-earthquake buildings using optical remote sensing images. Earthquake Engineering & Structural Dynamics. 2023; 52(11): 3392-3413.

[22]Xu Y, Qiao W, Zhao J. Vision-based multi-level synthetical evaluation of seismic damage for RC structural components: a multi-task learning approach. Earthquake Engineering and Engineering Vibration. 2023; 22(1): 69-85.

[23]Xu Y, Zhang C, Li H. Transformer-based large vision model for universal structural damage segmentation. Automation in Construction. 2025; 176: 106256.

[24]Wang Y, Jing X, Cui L. Geometric consistency enhanced deep convolutional encoder-decoder for urban seismic damage assessment by UAV images. Engineering Structures. 2023; 286: 116132.

[25]Cheng C S, Behzadan A H, Noshadravan A. Deep learning for post-hurricane aerial damage assessment of buildings. Computer-Aided Civil and Infrastructure Engineering. 2021; 36(6): 695-710.

[26]Janalipour M, Mohammadzadeh A. A fuzzy-ga based decision making system for detecting damaged buildings from high-spatial resolution optical images. Remote Sensing. 2017; 9(4): 349.

[27]Yu X, Hu X, Wang G. Machine-Learning Estimation of Snow Depth in 2021 Texas Statewide Winter Storm Using SAR Imagery. Geophysical Research Letters. 2022; 49(17): e2022GL099119.

[28]Liu Y, Chen D, Ma A. Multiscale U-shaped CNN building instance extraction framework with edge constraint for high-spatial-resolution remote sensing imagery. IEEE Transactions on Geoscience and Remote Sensing. 2020; 59(7): 6106-6120.

[29]Chen L C, Papandreou G, Kokkinos I. Deeplab: Semantic image segmentation with deep convolutional nets, atrous convolution, and fully connected crfs. IEEE Transactions on Pattern Analysis and Machine Intelligence. 2017; 40(4): 834-848.

[30]Lin F, Hu X, Lin Y. Dual-branch multi-modal convergence network for crater detection using Chang'e image. International Journal of Applied Earth Observation and Geoinformation. 2024; 134: 104215.

[31]Hao H, Baireddy S, Bartusiak E R. An attention-based system for damage assessment using satellite imagery. IEEE International Geoscience and Remote Sensing Symposium. 2021: 4396-4399.

[32]Shen Y, Zhu S, Yang T. Bdanet: Multiscale convolutional neural network with cross-directional attention for building damage assessment from satellite images. IEEE Transactions on Geoscience and Remote Sensing. 2021; 60: 1-14.

[33]Zhao H, Shi J, Qi X. Pyramid scene parsing network. Proceedings of the IEEE Conference on Computer Vision and Pattern Recognition. 2017: 2881-2890.

[34]Liu Y, Gross L, Li Z. Automatic building extraction on high-resolution remote sensing imagery using deep convolutional encoder-decoder with spatial pyramid pooling. IEEE Access. 2019; 7: 128774-128786.

[35]Gupta R, Hosfelt R, Sajeev S. xbd: A dataset for assessing building damage from satellite imagery. ArXiv Preprint ArXiv:1911.09296. 2019.

[36]Yasin M Y, Abdullah J, Noor N M. Landsat observation of urban growth and land use change using NDVI and NDBI analysis. IOP Conference Series: Earth and Environmental Science. 2022; 1067(1): 012037.

[37]Tay C W J, Yun S H, Chin S T. Rapid flood and damage mapping using synthetic aperture radar in response to Typhoon Hagibis, Japan. Scientific Data. 2020; 7(1): 100.

[38]Miglietta M M, Rotunno R. Development mechanisms for Mediterranean tropical-like cyclones (medicanes). Quarterly Journal of the Royal Meteorological Society. 2019; 145(721): 1444-1460.
[39]Fowler H J, Blenkinsop S, Green A. Precipitation extremes in 2023. Nature Reviews Earth & Environment. 2024; 5(4): 250-252.
[40]Drusch M, Del Bello U, Carlier S. Sentinel-2: ESA's optical high-resolution mission for GMES operational services. Remote Sensing of Environment. 2012; 120: 25-36.
[41]Adrah E, Wong J P, Yin H. Integrating GEDI, Sentinel-2, and Sentinel-1 imagery for tree crops mapping. Remote Sensing of Environment. 2025; 319: 114644.
[42]Tarpanelli A, Mondini A C, Camici S. Effectiveness of Sentinel-1 and Sentinel-2 for flood detection assessment in Europe. Natural Hazards and Earth System Sciences. 2022; 22(8): 2473-2489.
[43]Konapala G, Kumar S V, Ahmad S K. Exploring Sentinel-1 and Sentinel-2 diversity for flood inundation mapping using deep learning. ISPRS Journal of Photogrammetry and Remote Sensing. 2021; 180: 163-173.
[44]Aimaiti Y, Sanon C, Koch M. War related building damage assessment in Kyiv, Ukraine, using Sentinel-1 radar and Sentinel-2 optical images. Remote Sensing. 2022; 14(24): 6239.
[45]Putri A F S, Widyatmanti W, Umarhadi D A. Sentinel-1 and Sentinel-2 data fusion to distinguish building damage level of the 2018 Lombok Earthquake. Remote Sensing Applications: Society and Environment. 2022; 26: 100724.
[46]Fielding E J, Jung J. Damage Proxy Mapping with SAR interferometric coherence change. Procedia Computer Science. 2024; 239: 2322-2328.
[47]Zha Y, Gao J, Ni S. Use of normalized difference built-up index in automatically mapping urban areas from TM imagery. International Journal of Remote Sensing. 2003; 24(3): 583-594.
[48]Ehrlich D, Freire S, Melchiorri M. Open and consistent geospatial data on population density, built-up and settlements to analyse human presence, societal impact and sustainability: A review of GHSL applications. Sustainability. 2021; 13(14): 7851.
[49]Zheng Z, Zhong Y, Wang J, et al. Building damage assessment for rapid disaster response with a deep object-based semantic change detection framework: From natural disasters to man-made disasters. Remote Sensing of Environment. 2021; 265: 112636.
[50]Chen H, Nemni E, Vallecorsa S, et al. Dual-tasks siamese transformer framework for building damage assessment. IEEE International Geoscience and Remote Sensing Symposium. 2022; 1600-1603.
[51]Chen G, Li L, Dai Y, et al. AAU-net: an adaptive attention U-net for breast lesions segmentation in ultrasound images[J]. IEEE Transactions on Medical Imaging, 2022, 42(5): 1289-1300.
[52]Jin X, Guo C, He Z, et al. FCMNet: Frequency-aware cross-modality attention networks for RGB-D salient object detection[J]. Neurocomputing, 2022, 491: 414-425.
[53]Genovese E. A methodological approach to land use-based flood damage assessment in urban areas: Prague case study. Technical EUR Reports. 2006: 22497.
[54]Jiang Y, Yuan F, Farahmand H. Data-driven tracking of the bounce-back path after disasters: Critical milestones of population activity recovery and their spatial inequality. International Journal of Disaster Risk Reduction. 2023; 92: 103693.
[55]Zhu Z. Change detection using landsat time series: A review of frequencies, preprocessing, algorithms, and applications. ISPRS Journal of Photogrammetry and Remote Sensing. 2017; 130: 370-384.
[56]He K, Zhang X, Ren S. Deep residual learning for image recognition. Proceedings of the IEEE Conference on Computer Vision and Pattern Recognition. 2016: 770-778.
[57]He K, Zhang X, Ren S. Spatial pyramid pooling in deep convolutional networks for visual recognition. IEEE Transactions on Pattern Analysis and Machine Intelligence. 2015; 37(9): 1904-1916.
[58]Yu B, Yang L, Chen F. Semantic segmentation for high spatial resolution remote sensing images based on convolution neural network and pyramid pooling module. IEEE Journal of Selected Topics in Applied Earth Observations and Remote Sensing. 2018; 11(9): 3252-3261.
[59]Polak M, Zhang H, Pi M. An evaluation metric for image segmentation of multiple objects. Image and Vision Computing. 2009; 27(8): 1223-1227.
[60]Abdi G, Jabari S. A multi-feature fusion using deep transfer learning for earthquake building damage detection. Canadian Journal of Remote Sensing. 2021; 47(2): 337-352.
[61]Yun S, Han D, Oh S J. Cutmix: Regularization strategy to train strong classifiers with localizable features. Proceedings of the IEEE/CVF International Conference on Computer Vision. 2019: 6023-6032.
[62]Xia H ,Wu J ,Yao J. A Deep Learning Application for Building Damage Assessment Using Ultra-High-Resolution Remote Sensing Imagery in Turkey Earthquake. International Journal of Disaster Risk Science. 2023; 14(06): 947-962.
[63]Javed A, Cheng Q, Peng H. Review of spectral indices for urban remote sensing. Photogrammetric Engineering & Remote Sensing. 2021; 87(7): 513-524.
[64]Touzi R, Lopes A, Bruniquel J. Coherence estimation for SAR imagery. IEEE Transactions on Geoscience and Remote Sensing. 1999; 37(1): 135-149.
[65]Yu X, Hu X, Wang G. Machine-Learning Estimation of Snow Depth in 2021 Texas Statewide Winter Storm Using SAR Imagery. Geophysical Research Letters. 2022; 49(17): e2022GL099119.
[66]Pulvirenti L, Chini M, Pierdicca N. Use of SAR data for detecting floodwater in urban and agricultural areas: The role of the interferometric coherence. IEEE Transactions on Geoscience and Remote Sensing. 2015; 54(3): 1532-1544.
[67]Nico G, Pappalepore M, Pasquariello G. Comparison of SAR amplitude vs. coherence flood detection methods-a GIS application. International Journal of Remote Sensing. 2000; 21(8): 1619-1631.
[68]Li Y, Martinis S, Plank S. An automatic change detection approach for rapid flood mapping in Sentinel-1 SAR data. International Journal of Applied Earth Observation and Geoinformation. 2018; 73: 123-135.
[69]Yun S H, Hudnut K, Owen S. Rapid damage mapping for the 2015 M w 7.8 Gorkha earthquake using synthetic aperture radar data from COSMO–SkyMed and ALOS-2 Satellites. Seismological Research Letters. 2015; 86(6): 1549-1556.
[70]Fielding E J, Jung J. Damage Proxy Mapping with SAR interferometric coherence change. Procedia Computer Science. 2024; 239: 2322-2328.
[71]Portalés-Julià E, Mateo-García G, Purcell C. Global flood extent segmentation in optical satellite images. Scientific Reports. 2023; 13(1): 20316.
[72]Moreira A, Prats-Iraola P, Younis M, et al. A tutorial on synthetic aperture radar. IEEE Geoscience and Remote Sensing Magazine. 2013; 1(1): 6-43.